Editors' Suggestion

Simultaneous determination of local magnetic fields and sensor orientation with nitrogen-vacancy centers in nanodiamond

Yizhou Wang,[1,*] Haochen Shen,[1,*] Zhongyuan Liu,[1] Yue Yu,[1] Shengwang Du,[2,3,4] Chong Zu,[1,5,†] and Chuanwei Zhang[1,5,‡]

[1]*Department of Physics, Washington University in St. Louis. St. Louis, Missouri, USA*
[2]*Elmore Family School of Electrical and Computer Engineering, Purdue University, West Lafayette, Indiana, USA*
[3]*Department of Physics and Astronomy, Purdue University, West Lafayette, Indiana, USA*
[4]*Purdue Quantum Science and Engineering Institute, Purdue University, West Lafayette, Indiana, USA*
[5]*Center for Quantum Leaps, Washington University, St. Louis, Missouri, USA*

(Received 17 April 2026; accepted 3 September 2026; published 28 October 2026)

Nitrogen-vacancy (NV) centers in nanodiamonds have emerged as a promising quantum sensing platform for biomedical imaging applications, yet random orientations of individual particles present significant challenges in large-scale sensor calibration. In this study, we demonstrate a novel approach to simultaneously determine each particle's crystallographic axes and the surrounding local vector magnetic field. Specifically, a minimum of four distinct bias fields is required to unambiguously extract both the orientation and the local field. We validate our method experimentally using NV centers in two scenarios: (i) in a bulk diamond with known crystal orientation as a proof of concept and (ii) on various single nanodiamonds to mimic real-world applications. Our work represents a crucial step toward unlocking the full potential of nanodiamonds for advanced applications such as *in situ* biomedical imaging and nanoscale sensing in complex environments.

DOI: 10.1103/zh44-55ms

I. INTRODUCTION

Quantum sensing with nitrogen-vacancy (NV) centers in diamond has enabled measurements of magnetic [1–8], electric [9–11], chemical [12–14], and thermal signals [15–19] at the nanoscale, with applications spanning condensed matter physics [20–25], quantum technology [26–28], and biomedicine [29–34]. A core strength of NV centers lies in their ability to reveal vector magnetic field information through optically detected magnetic resonance (ODMR), a technique that exploits spin-dependent fluorescence to track electron spin transitions [35,36].

However, extending NV-based magnetometry to biologically relevant contexts presents unique challenges, primarily due to the random orientations of NV-containing nanodiamonds when dispersed within complex environments like cells and tissues [37–39]. Previous studies have demonstrated the feasibility of orientation tracking [40] in biological systems using ODMR spectra, achieving subdegree angular resolutions [38], full tomographic orientation reconstruction via modulated external magnetic fields [41], and simultaneous tracking of rotational and translational movement [30]. Despite these advances, the current orientation tracking approach typically relies on the assumption that "the external magnetic fields at their positions are well known" [42]. This interdependency—where magnetometry requires known orientation, and orientation determination relies on known fields—poses considerable challenges for robust orientation sensing and magnetometry when the local-field signals from the target sample, such as those from ferritin [43,44], are present and unknown.

Our approach directly addresses this challenge. We demonstrate that a minimum of four independent ODMR measurements, under appropriately chosen bias field configurations, are sufficient to reconstruct both the full local vector magnetic field and the NV orientations. This congruence is significant: it matches the number of measurements previously established for determining only the NV axes when external magnetic fields are well characterized [41], suggesting that comprehensive information (both local field and orientation) can be efficiently extracted with a comparable measurement overhead.

The paper is organized as follows: First, we detail the theory and methodology underpinning our approach in Secs. II and III, including the Hamiltonian for the NV center and the mathematical formulation for reconstructing orientation and field parameters from ODMR spectra

[*]These authors contributed equally to this work.
[†]Contact author: zu@wustl.edu
[‡]Contact author: chuanwei.zhang@wustl.edu

 © 2026 American Physical Society

under multiple bias fields. Second, we describe the experimental validations (Sec. IV) and numerical simulations (Sec. V) of our method. This includes proof-of-concept experiments on a bulk-diamond crystal with known NV orientations, followed by experiments on various single nanodiamonds where both orientation and local field are unknown. We compare experimental findings with corresponding numerical simulations for both scenarios. Finally, we conduct a noise analysis, investigating the impact of factors such as the number and strength of bias magnetic fields and experimental noise from finite ODMR linewidth and photon shot noise. We conclude with a discussion of our findings and potential avenues for further research in Sec. VI.

II. METHODOLOGIES AND FRAMEWORKS

Having outlined the paper's structure, we now describe the physical platform and analysis workflow in detail. Figure 1 provides an overview: Panel (a) sketches the wide-field ODMR microscope used in this study and, in the inset, shows two representative single-crystal nanodiamond particles approximately 750 nm in diameter. Each particle hosts an ensemble of negatively charged NV centers that function as local vector magnetometers. Sample-preparation details are provided in Supplemental Material [45]. The sensing element itself is governed by the ground-state spin-1 Hamiltonian [32,47] depicted in panel (b),

$$\hat{H} = D_{\mathrm{gs}}\, S_z^2 + \gamma_e\, (\vec{B}\cdot\vec{S}), \tag{1}$$

where $D_{\mathrm{gs}} = (2\pi)\times 2.87$ GHz is the zero-field splitting, $\gamma_e = (2\pi)\times 28.0$ MHz/mT is the gyromagnetic ratio, $\vec{B}$ is the vector magnetic field, and $\vec{S}$ is the spin-1 operator for the NV center. Here we assume the magnetic field is the dominant signal and neglect the small local strain- and electric-field-induced mixing between the $|m_s = \pm 1\rangle$ levels. The resulting energy of the three NV spin levels could be obtained by solving the eigenvalues using the matrix form

$$\lambda[(D-\lambda)^2 - \mu_e^2(B^{\mathrm{proj}})^2] - (\lambda - D)\mu_e^2[(B^{\mathrm{tot}})^2 - (B^{\mathrm{proj}})^2] = 0, \tag{2}$$

where λ are the spin state energies, B^{tot} is the magnitude of the total magnetic field (including the applied bias magnetic field and the local field from the environment that we would like to sense), and B^{proj} is the total magnetic field's projection on the specific NV axis.

The ODMR spectrum measures the two microwave transitions from $|m_s = 0\rangle$ to the $|m_s = \pm 1\rangle$ levels, and the splitting between the two resonances can be calculated as $(\lambda_{+1} - \lambda_{-1})$ by fitting the spectrum using a Monte Carlo multistart fitting procedure (see Supplemental Material [45]). For a single-crystal nanodiamond containing an ensemble of NV centers, the NV axes can align along four crystallographic directions [Fig. 1(c)]. The resulting ODMR spectrum typically exhibits four pairs of resonances with splittings that are, to leading order, proportional to the magnetic field projection, B^{proj}, onto each NV axis [Fig. 1(b)]. We label the four NV axis as $\hat{n}_1$, $\hat{n}_2$, $\hat{n}_3$, and $\hat{n}_4$ (see Eq. (S3) in Supplemental Material [45]).

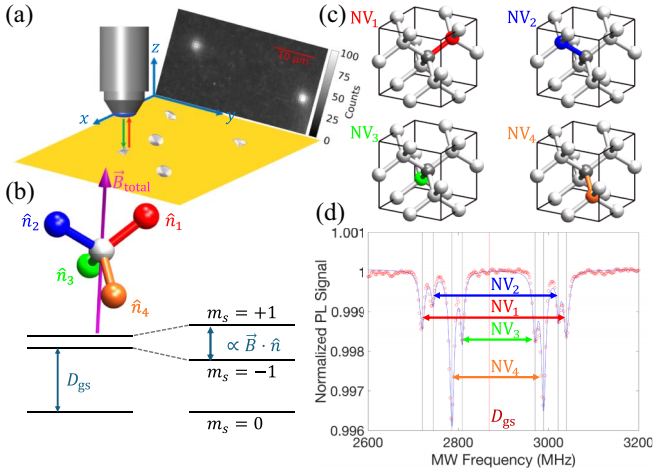


FIG. 1. Introduction to NV centers in nanodiamonds. (a) Schematic of an experimental setup for imaging NV centers in diamond crystals. The lab frame coordinate axes x, y, and z are indicated in blue. The inset shows an optical fluorescence image of two single-crystal nanodiamond particles approximately 750 nm in diameter. When excited by a 532-nm laser, the NV centers emit red fluorescence comprising a zero-phonon line at 637 nm and a broad phonon sideband extending to approximately 800 nm. (b) Energy-level structure of the NV center ground state under an external magnetic field. The Zeeman splitting between $m_s = \pm 1$ states is proportional (to first order) to $\vec{B}\cdot\hat{n}$, where $\hat{n}$ is the NV axis direction and $\vec{B}$ is the magnetic field at the diamond. (c) Atomic models of the four possible NV center orientations ($NV_1 \rightarrow NV_4$) within the diamond lattice, each corresponding to a different crystallographic direction and colored uniquely (red, blue, green, and orange, respectively). (d) A typical optically detected magnetic resonance (ODMR) spectrum from a single nanodiamond showing characteristic resonance peaks corresponding to the four NV orientations, with the splitting magnitude proportional (to first order) to the projection of the magnetic field along each NV axis.

We also note that the total magnetic field can be further decomposed into $\vec{B}^{\,\mathrm{tot}} = \vec{B}^{\,\mathrm{bias}} + \vec{B}^{\,\mathrm{loc}}$, where $\vec{B}^{\,\mathrm{bias}}$ denotes the bias magnetic field we applied externally and $\vec{B}^{\,\mathrm{loc}}$ being the local magnetic field in the environment that we want to sense. Thus, the magnetic fields in the laboratory frame (labeled by coordinate $\{\hat{x}, \hat{y}, \hat{z}\}$) can be projected to the NV frame by

$$\hat{n}_j \cdot (\vec{B}^{\,\mathrm{bias}} + \vec{B}^{\,\mathrm{loc}}) = B_j^{\mathrm{proj}}, \tag{3}$$

where $j = 1, 2, 3, 4$ represents the unit vectors of the four possible NV symmetry axes.

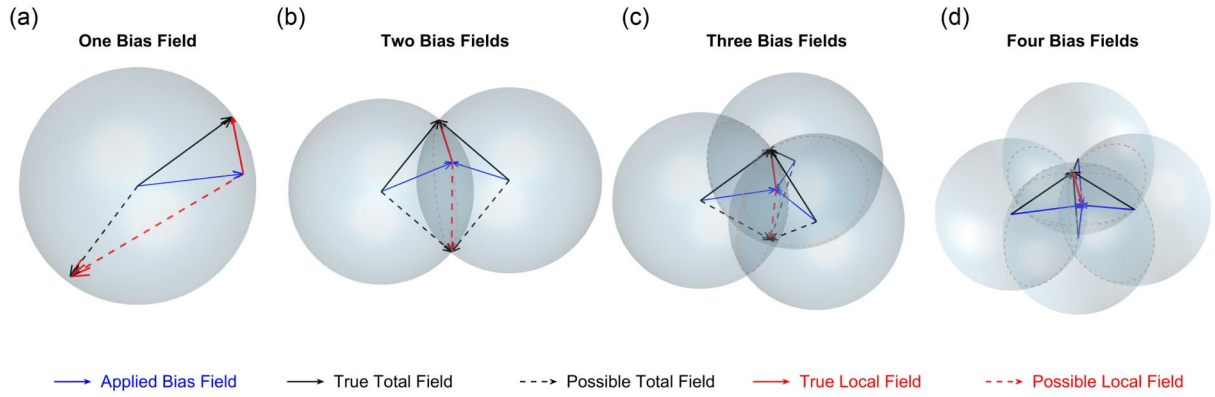


FIG. 2. Illustration of the process for determining the local magnetic field and NV center orientation using multiple bias magnetic fields. (a) When a single bias field B_1^{bias} is applied, the possible solutions of B^{loc} form a sphere (resembled by the two red arrows), making the local field undetermined. (b) With a second nonparallel bias field B_2^{bias}, the solution space reduces to a ring (red dashed curve) at the intersection of two spheres. However, the local field is still ambiguous. (c) A third bias field B_3^{bias} further constrains the possible solutions to two mirror-symmetric points, as shown by the solid and dashed red arrows pointing upward and downward correspondingly. This symmetry introduces a degeneracy that prevents a unique determination of the local field. (d) In the case of four bias fields, this degeneracy is resolved.

We will apply a series of bias magnetic fields and measure the corresponding ODMR splittings for all NV groups [Fig. 1(d)]. By choosing the non-coplanar bias fields like we described in Sec. III, plugging Eq. (3) into Eq. (2) and solving these simultaneously, we can obtain the corresponding local magnetic field and nanodiamond crystallographic orientation in the lab frame. Considering it is a set of nonlinear equations with multiple unknowns, instead of solving the equations directly, we change that into an optimization problem and opt to use MATLAB Multistart [48].

III. MINIMUM NUMBER OF BIAS MAGNETIC FIELDS

A crucial aspect of our method is determining the minimum number of $\vec{B}^{\,\text{bias}}$ required to extract both NV orientation and the local field, $\vec{B}^{\,\text{loc}}$. Given that each NV center has a unique orientation in the nanodiamond, $\vec{B}^{\,\text{loc}}$ can only be reconstructed when sufficient constraints are imposed by $\vec{B}^{\,\text{bias}}$, as analyzed below.

Single bias field: Our framework starts by setting the unknown local field $\vec{B}^{\,\text{loc}}$ as a fixed vector originating at the coordinate (0, 0, 0) in the lab frame [Fig. 2(a)]. When a single bias magnetic field B_1^{bias} is applied, the only directly obtainable quantity is the magnitude of the total field $|\vec{B}_1^{\,\text{tot}}|$ (see Supplementary Material [45]), while orientation remains undetermined. Specifically, the $\vec{B}_1^{\,\text{tot}} = \vec{B}_1^{\,\text{bias}} + \vec{B}^{\,\text{loc}}$ can reside anywhere on a sphere with center at $(-B_x^{\text{bias}}, -B_y^{\text{bias}}, -B_z^{\text{bias}})$ and radius as the magnitude of $\vec{B}_1^{\,\text{tot}}$, thus leaving the determination of $\vec{B}^{\,\text{loc}}$ impossible.

Two bias fields: By applying a second $\vec{B}_2^{\,\text{bias}}$ which is not parallel to the first bias field, we impose a second constraint:

$$\begin{aligned} |\vec{B}_1^{\,\text{bias}} + \vec{B}^{\,\text{loc}}| &= |\vec{B}_1^{\,\text{total}}| \\ |\vec{B}_2^{\,\text{bias}} + \vec{B}^{\,\text{loc}}| &= |\vec{B}_2^{\,\text{total}}| \end{aligned} \tag{4}$$

Geometrically, this restricts the set of possible $\vec{B}^{\,\text{loc}}$ to a ring-shaped intersection of the two spheres, as depicted in Fig. 2(b). While this additional constraint reduces the number of possible solutions, it is still not sufficient to uniquely determine $\vec{B}^{\,\text{loc}}$.

Three bias fields: Introducing a third $\vec{B}_3^{\,\text{bias}}$ that is not in the same plane as the prior two bias fields, we can further restrict the possible $\vec{B}^{\,\text{loc}}$ to two points, as illustrated in Fig. 2(c). This occurs because the intersection of three spheres generally results in two solutions that are symmetric about the plane formed by the centers of three spheres.

Four bias fields: To resolve this twofold degeneracy, we apply a fourth non-coplanar $\vec{B}_4^{\,\text{bias}}$ (i.e., the centers of the four spheres do not lie in the same plane), as shown in Fig. 2(d). Interestingly, four bias fields is also the minimum number needed to determine solely the nanodiamond axes in the absence of the unknown $\vec{B}^{\,\text{loc}}$ [41]. As a result, four bias fields are sufficient to simultaneously determine $\vec{B}^{\,\text{loc}}$ and nanodiamond orientation.

Subsequent numerical simulations and experimental validation confirm this necessity: with three bias fields, there remains a symmetry-induced ambiguity, while four bias fields consistently produce unique solutions for determining local magnetic fields.

IV. EXPERIMENTAL VALIDATION

Two experimental configurations are used here:

(i) A bulk diamond with known crystal orientation: the NV axes are well characterized, allowing us to validate the accuracy of our method in a controlled environment.
(ii) Single nanodiamond: mimicking real-world applications, where the NV axes are random and unknown. The method is tested for robustness in reconstructing these parameters.

We first perform measurements on a [100]-cut plate diamond, with the four NV-axis orientations known *a priori* and given by

$$\begin{aligned}\hat{n}_1 &= [+\sqrt{2}, 0, +1]/\sqrt{3};\\ \hat{n}_2 &= [0, +\sqrt{2}, -1]/\sqrt{3};\\ \hat{n}_3 &= [-\sqrt{2}, 0, +1]/\sqrt{3};\\ \hat{n}_4 &= [0, -\sqrt{2}, -1]/\sqrt{3}.\end{aligned} \tag{5}$$

We apply 24 different bias fields, $\vec{B}^{\,\mathrm{bias}}$, each with a magnitude of approximately 1 mT using three-dimensional electromagnetic coils. Care was taken to ensure the applied bias fields were not coplanar to avoid degeneracies in the reconstruction.

As a calibration, we tested whether our method could accurately reconstruct these known axes and determine $\vec{B}^{\,\mathrm{loc}}$ from the measured ODMR spectra. To quantify the stability of our reconstruction from different subsets of $\vec{B}^{\,\mathrm{bias}}$, we define two metrics:

(i) The standard deviation of the predicted $\vec{B}^{\,\mathrm{loc}}$:

$$\delta B_j^{\mathrm{loc}} = \sqrt{\frac{\sum (B_j^{\mathrm{loc}} - \bar{B}_j^{\mathrm{loc}})^2}{N}}, \tag{6}$$

where the summation is over a total of N reconstruction runs (each using a different subset of bias fields), $j = x, y, z$.

(ii) The standard deviation of the predicted axes orientations represented by the great circle distance, d_{gc}:

$$\begin{aligned}d_{\mathrm{gc}} = \frac{1}{N}\sum_{(\theta,\phi)} \cos^{-1}[&\cos(\theta)\cos(\bar{\theta})\cos(\phi - \bar{\phi})\\ &+ \sin(\theta)\sin(\bar{\theta})];\end{aligned} \tag{7}$$

Here (θ, ϕ) are the spherical coordinates representing a specific axis of NV (e.g., the first principal axis) determined in each run of reconstruction, and $(\bar{\theta}, \bar{\phi})$ are the mean spherical coordinates for that axis over the N runs.

For a proof-of-concept test, we choose $N = 50$ subsets of four randomly chosen bias field data and obtain the averaged NV-axis orientations to be (Fig. 3)

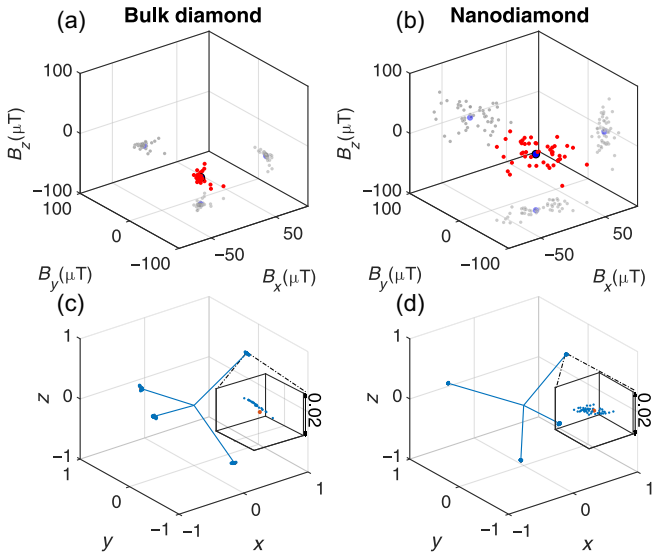


FIG. 3. Reconstructed local magnetic field (a),(b) and axes reconstruction (c),(d) using our method. Each column represents a different scenario: bulk-diamond experiment (a),(c) and nanodiamond experiment (b),(d). For each calculation shown, ten bias fields were randomly selected from the nanodiamond dataset and four from the bulk-diamond dataset. (a),(b) Reconstructed $\vec{B}^{\,\mathrm{loc}}$ values (red dots) are plotted with their projections on the yz, xz, and xy planes; the mean is marked by a blue dot. (c),(d) Reconstructed NV-axis orientations (solid lines) are compared with the ground truth for the bulk diamond or with the mean orientation for the nanodiamond. The inset cubes magnify the distributions within a $0.02 \times 0.02 \times 0.02$ region around one predicted axis. Panels (a),(c) show sub-2 μT bulk-diamond field consistency and high-axis fidelity, whereas panels (b),(d) show approximately 50 μT nanodiamond field consistency and approximately 1° axis consistency.

$$\begin{aligned}\hat{n}_1^{\mathrm{exp}} &= \hat{n}_1 - 0.0061\,\hat{x} - 0.0051\,\hat{y} + 0.0085\,\hat{z}\\ \hat{n}_2^{\mathrm{exp}} &= \hat{n}_2 + 0.0013\,\hat{x} + 0.0095\,\hat{y} + 0.0137\,\hat{z}\\ \hat{n}_3^{\mathrm{exp}} &= \hat{n}_3 - 0.0061\,\hat{x} - 0.0142\,\hat{y} - 0.0088\,\hat{z}\\ \hat{n}_4^{\mathrm{exp}} &= \hat{n}_4 + 0.0108\,\hat{x} + 0.0098\,\hat{y} - 0.0135\,\hat{z}\end{aligned} \tag{8}$$

The reconstructed axes agree well with the known bulk-diamond crystal orientation [Eq. (5)], with a mean angular deviation of $d_{\mathrm{gc}} < 0.5°$.

Simultaneously, we obtain the local field

$$\vec{B}^{\,\mathrm{loc}} = [-2.5, -14.9, -53.2] \pm [1.0, 1.1, 1.4]\ \mu\mathrm{T}.$$

The uncertainties represent the standard deviation (δB) across multiple reconstruction runs. $\vec{B}^{\,\mathrm{loc}}$ closely matches the geomagnetic field in the U.S. Midwest [49], highlighting the precision of our method.

We next extend our protocol to NV centers embedded in individual nanodiamonds, a more demanding setting where the crystal orientation is unknown *a priori*. In nanodiamonds, the ODMR resonances are substantially

broadened (full width half maximum, FWHM ~ 10 MHz) compared to bulk diamond (FWHM ~ 0.6 MHz), resulting in elevated noise floors and increased uncertainty in parameter extraction. To mitigate this, we apply 34 different bias magnetic fields with magnitudes of approximately 5–10 mT to better separate the eight resonances. Reconstruction is then performed by randomly selecting subsets of these fields.

Using four bias fields per run, the consistency in axes prediction remains high, with d_{gc} typically around 1°. However, the prediction for the local field $\vec{B}^{loc}$ exhibits significantly greater variation than in bulk diamond due to the broader ODMR linewidth. To improve the field accuracy, we increase the number of bias fields per run. Figure 3(b) shows the average reconstructed $\vec{B}^{loc}$ using ten randomly selected bias field dataset, yielding $\vec{B}^{loc} = [-7, -33, -7] \pm [36, 11, 24]$ μT and a standard deviation δB of approximately 50 μT. This reduced precision arises primarily from the differing noise characteristics in bulk and nanodiamond ODMR spectra. Notably, our bulk diamond is isotopically purified to ^{13}C concentrations below 10^{-4} to suppress nuclear spin noise [50], while P1 centers and other paramagnetic defects provide additional plausible spin-bath contributions [51–53]. Moreover, the lower surface-to-volume ratio of bulk diamond reduces surface-spin and related defect-spin contributions relative to nanodiamonds [54,55]. As an additional cross-particle consistency check, we analyzed two different nanodiamonds on the same substrate and obtained local-field estimates that are consistent within experimental uncertainty (see Sec. *Consistency Checks* and corresponding supplementary figures in Supplemental Material [45]).

V. NUMERICAL ANALYSIS AND DISCUSSION

Finally, we perform simulations to quantify how experimental noise, strengths of bias fields, and the number of bias fields in one run affect the reconstruction accuracy. Starting from the bulk-diamond local field of around $\vec{B}^{loc} = 50$ μT pointing to $-z$ direction, we synthetically generate eight-peak ODMR spectra and add Gaussian noise with amplitudes between 0.1 and 0.5 MHz. Each noisy spectrum is fitted to locate the resonance frequencies, which are then passed to our reconstruction algorithm. For every noise level, we repeat the procedure with 4–10 bias-field configurations randomly selected from the 24 used in the bulk-diamond experiment. We perform an analogous analysis for nanodiamonds. Here the Gaussian noise amplitude is varied from 1 to 5 MHz, and 4–20 bias-field subsets are drawn from the 34 fields available in the experiment for each run.

The simulations uncover two clear trends (Fig. 4). First, the prediction errors, including both the local-field deviation, δB, and the angular deviation, d_{gc}, grow approximately linearly with the injected noise amplitude,

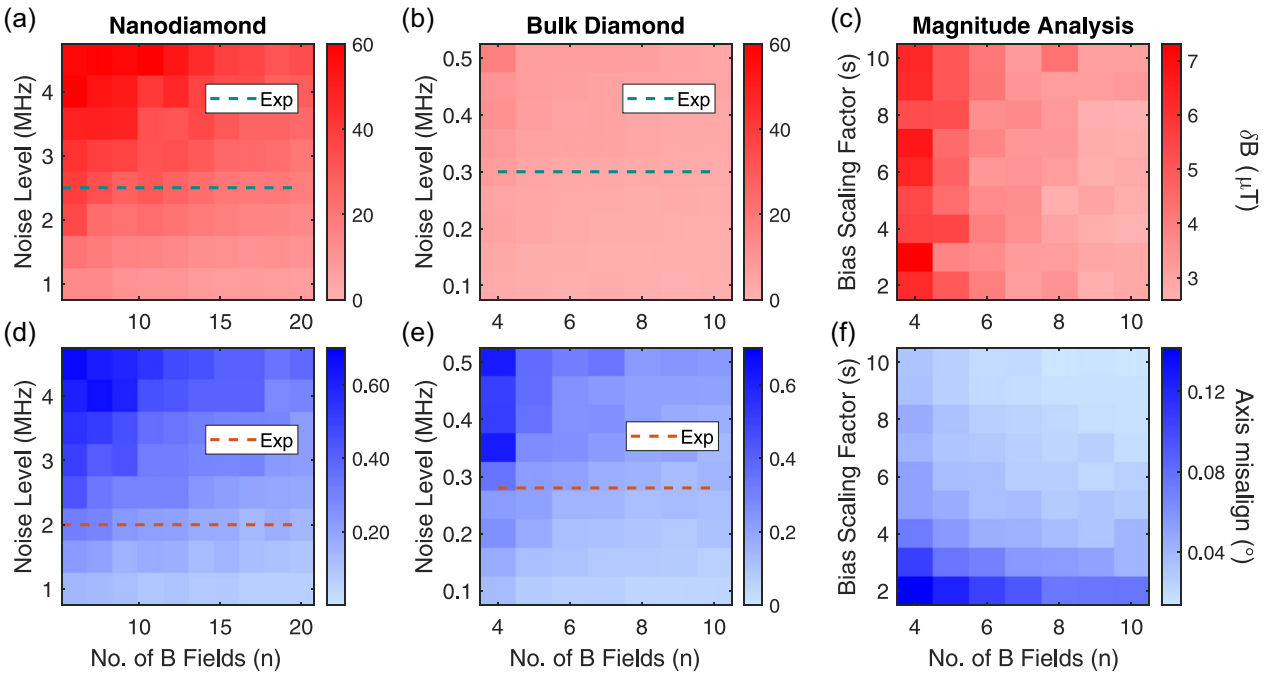


FIG. 4. Impact of noise, number of bias fields, and bias-field magnitude on reconstruction. The predictions for local fields are marked in red, axes in blue, and their corresponding experimental results in green and orange. (a),(b) Local-field deviation δB as a function of noise level and number of bias fields for the nanodiamond and bulk-diamond simulations, respectively. (d),(e) Axis misalignment d_{gc} for the corresponding nanodiamond and bulk-diamond simulations. (c),(f) Local-field deviation and axis misalignment, respectively, as functions of noise level and the overall bias-field scaling factor.

in agreement with standard error-propagation expectations. Second, adding more bias fields per reconstruction run improves accuracy, but the benefit saturates at around ten fields in the nanodiamond case. Simulations using bulk-diamond parameters exhibit the same qualitative behavior, but with uniformly smaller deviations owing to their lower noise level and thus higher signal-to-noise ratio in the ODMR spectra.

We also evaluate how bias-field strength influences reconstruction accuracy. Specifically, we carry out simulations in which all bias magnitudes are uniformly scaled by factors of 2–10 (denoted "Bias-Scaling Factor" in panels (c) and (f) of Fig. 4). Increasing the field strength noticeably enhances axis determination, yet yields only marginal improvement in the local-field error. This behavior can be intuitively understood using the geometrical picture in Fig. 2. Axis orientation is inferred indirectly from the relative directions of $\vec{B}^{\,\mathrm{bias}}$; with a fixed noise floor, scaling the bias magnitudes reduces the angular uncertainty and thus yields a reduced uncertainty in the axis estimate. By contrast, the local field $\vec{B}^{\,\mathrm{loc}}$ is extracted from the intersection point of the total field vectors. Once the bias field is already much larger than $\vec{B}^{\,\mathrm{loc}}$, further scaling hardly changes the absolute positional error, as it is set by the same noise floor.

VI. CONCLUSIONS AND OUTLOOKS

We have developed and experimentally validated a framework for simultaneously determining the NV center orientation and the local vector magnetic field. Our results show that at least four non-coplanar bias fields are required, consistent with previous orientation-only methods but enabling vector field reconstruction. The primary performance bottleneck of our protocol arises from the intrinsic noise inside nanodiamond sensors: ^{13}C nuclear spin bath, strain variations, and structural inhomogeneities. Addressing these noise sources is critical to improving the accuracy and reliability of our method under real-world conditions; approaches outlined in Refs. [5,56–62] offer viable solutions. In this experiment, we focus on the quasistatic regime, in which the nanodiamond orientation and local field are approximately constant over the spectra used for one reconstruction. Although the local field may depend on the applied bias field, even for ferritin-like moments, a low-field estimate suggests that bias-induced alignment is small under the present room-temperature, millitesla-field conditions [43,63]; systematically quantifying this dependence for other magnetic species and operating conditions is left for future work. Ultimately, we anticipate a robust, simultaneous readout of nanodiamond orientation and local magnetic fields will enable new classes of experiments, from tracking ferritin-related magnetic signatures in living systems [43,44] to diagnosing nanoscale magnetism in quantum materials.

ACKNOWLEDGMENTS

The authors acknowledge the support of NSF Grant No. 2503230 for enabling this research. C. Zu acknowledges support from NSF Expand-QISE 2328837. C. Zhang acknowledges support from NSF ECCS-2411394.

DATA AVAILABILITY

There are no publicly available research data or software supporting this manuscript. Requests for further information or data should be sent to the authors.

[1] G. Balasubramanian, I. Y. Chan, R. Kolesov, M. Al-Hmoud, J. Tisler, C. Shin, C. Kim, A. Wojcik, P. R. Hemmer, A. Krueger, T. Hanke, A. Leitenstorfer, R. Bratschitsch, F. Jelezko, and J. Wrachtrup, Nanoscale imaging magnetometry with diamond spins under ambient conditions, Nature (London) **455**, 648 (2008).

[2] J. R. Maze, P. L. Stanwix, J. S. Hodges, S. Hong, J. M. Taylor, P. Cappellaro, L. Jiang, M. V. G. Dutt, E. Togan, A. S. Zibrov, A. Yacoby, R. L. Walsworth, and M. D. Lukin, Nanoscale magnetic sensing with an individual electronic spin in diamond, Nature (London) **455**, 644 (2008).

[3] V. M. Acosta, E. Bauch, M. P. Ledbetter, C. Santori, K.-M. C. Fu, P. E. Barclay, R. G. Beausoleil, H. Linget, J. F. Roch, F. Treussart, S. Chemerisov, W. Gawlik, and D. Budker, Diamonds with a high density of nitrogen-vacancy centers for magnetometry applications, Phys. Rev. B **80**, 115202 (2009).

[4] R. S. Schoenfeld and W. Harneit, Real time magnetic field sensing and imaging using a single spin in diamond, Phys. Rev. Lett. **106**, 030802 (2011).

[5] E. T. Güldeste and C. Bulutay, Wavelet-based Ramsey magnetometry enhancement of a single $\mathrm{N}-v$ center in diamond, Phys. Rev. Appl. **22**, 044030 (2024).

[6] J. F. Barry, J. M. Schloss, E. Bauch, M. J. Turner, C. A. Hart, L. M. Pham, and R. L. Walsworth, Sensitivity optimization for NV-diamond magnetometry, Rev. Mod. Phys. **92**, 015004 (2020).

[7] A. Jarmola, V. M. Acosta, K. Jensen, S. Chemerisov, and D. Budker, Temperature- and magnetic-field-dependent longitudinal spin relaxation in nitrogen-vacancy ensembles in diamond, Phys. Rev. Lett. **108**, 197601 (2012).

[8] H. Huang, H. Dong, L. Chen, and Y. Gao, Single-beam three-axis atomic magnetometer, Appl. Phys. Lett. **109**, 062404 (2016).

[9] F. Dolde, H. Fedder, M. W. Doherty, T. Nöbauer, F. Rempp, G. Balasubramanian, T. Wolf, F. Reinhard, L. C. L. Hollenberg, F. Jelezko, and J. Wrachtrup, Electric-field sensing using single diamond spins, Nat. Phys. **7**, 459 (2011).

[10] M. Block, B. Kobrin, A. Jarmola, S. Hsieh, C. Zu, N. L. Figueroa, V. M. Acosta, J. Minguzzi, J. R. Maze, D. Budker, and N. Y. Yao, Optically enhanced electric field sensing using nitrogen-vacancy ensembles, Phys. Rev. Appl. **16**, 024024 (2021).

[11] J. M. Taylor, P. Cappellaro, L. Childress, L. Jiang, D. Budker, P. R. Hemmer, A. Yacoby, R. Walsworth, and M. D. Lukin, High-sensitivity diamond magnetometer with nanoscale resolution, Nat. Phys. **4**, 810 (2008).

[12] R. Igarashi, Y. Yoshinari, H. Yokota, T. Sugi, F. Sugihara, K. Ikeda, H. Sumiya, S. Tsuji, I. Mori, H. Tochio, Y. Harada, and M. Shirakawa, Real-time background-free selective imaging of fluorescent nanodiamonds in vivo, Nano Lett. **12**, 5726 (2012).

[13] T. Fujisaku, R. Tanabe, S. Onoda, R. Kubota, T. F. Segawa, F. T.-K. So, T. Ohshima, I. Hamachi, M. Shirakawa, and R. Igarashi, pH nanosensor using electronic spins in diamond, ACS Nano **13**, 11726 (2019).

[14] T. Rendler, J. Neburkova, O. Zemek, J. Kotek, A. Zappe, Z. Chu, P. Cigler, and J. Wrachtrup, Optical imaging of localized chemical events using programmable diamond quantum nanosensors, Nat. Commun. **8**, 14701 (2017).

[15] V. M. Acosta, E. Bauch, M. P. Ledbetter, A. Waxman, L.-S. Bouchard, and D. Budker, Temperature dependence of the nitrogen-vacancy magnetic resonance in diamond, Phys. Rev. Lett. **104**, 070801 (2010).

[16] X.-D. Chen, C.-H. Dong, F.-W. Sun, C.-L. Zou, J.-M. Cui, Z.-F. Han, and G.-C. Guo, Temperature dependent energy level shifts of nitrogen-vacancy centers in diamond, Appl. Phys. Lett. **99**, 161903 (2011).

[17] D. M. Toyli, D. J. Christle, A. Alkauskas, B. B. Buckley, C. G. Van de Walle, and D. D. Awschalom, Measurement and control of single nitrogen-vacancy center spins above 600 K, Phys. Rev. X **2**, 031001 (2012).

[18] T. Yanagi, K. Kaminaga, W. Kada, O. Hanaizumi, and R. Igarashi, Optimization of wide-field ODMR measurements using fluorescent nanodiamonds to improve temperature determination accuracy, Nanomaterials **10**, 2282 (2020).

[19] G. Kucsko, P. C. Maurer, N. Y. Yao, M. Kubo, H. J. Noh, P. K. Lo, H. Park, and M. D. Lukin, Nanometre-scale thermometry in a living cell, Nature (London) **500**, 54 (2013).

[20] F. Casola, T. van der Sar, and A. Yacoby, Probing condensed matter physics with magnetometry based on nitrogen-vacancy centres in diamond, Nat. Rev. Mater. **3**, 1 (2018).

[21] S. Hsieh, P. Bhattacharyya, C. Zu, T. Mittiga, T. J. Smart, F. Machado, B. Kobrin, T. O. Höhn, N. Z. Rui, M. Kamrani, S. Chatterjee, S. Choi, M. Zaletel, V. V. Struzhkin, J. E. Moore, V. I. Levitas, R. Jeanloz, and N. Y. Yao, Imaging stress and magnetism at high pressures using a nanoscale quantum sensor, Science **366**, 1349 (2019).

[22] M. J. Ku, T. X. Zhou, Q. Li, Y. J. Shin, J. K. Shi, C. Burch, L. E. Anderson, A. T. Pierce, Y. Xie, A. Hamo *et al.*, Imaging viscous flow of the Dirac fluid in graphene, Nature (London) **583**, 537 (2020).

[23] P. Bhattacharyya *et al.*, Imaging the Meissner effect in hydride superconductors using quantum sensors, Nature (London) **627**, 73 (2024).

[24] Z. Liu, R. Gong, J. Kim, O. K. Diessel, Q. Xu, Z. Rehfuss, X. Du, G. He, A. Singh, Y. S. Eo, E. A. Henriksen, G. D. Gu, N. Y. Yao, F. Machado, S. Ran, S. Chatterjee, and C. Zu, Quantum noise spectroscopy of superconducting dynamics in thin film $Bi_2Sr_2CaCu_2O_{8+\delta}$, arXiv:2502.04439.

[25] Q.-C. Sun, T. Song, E. Anderson, A. Brunner, J. Förster, T. Shalomayeva, T. Taniguchi, K. Watanabe, J. Gräfe, R. Stöhr *et al.*, Magnetic domains and domain wall pinning in atomically thin $CrBr_3$ revealed by nanoscale imaging, Nat. Commun. **12**, 1989 (2021).

[26] C. Zu, W.-B. Wang, L. He, W.-G. Zhang, C.-Y. Dai, F. Wang, and L.-M. Duan, Experimental realization of universal geometric quantum gates with solid-state spins, Nature (London) **514**, 72 (2014).

[27] H. Gao, L. S. Martin, L. B. Hughes, N. T. Leitao, P. Put, H. Zhou, N. U. Koyluoglu, S. A. Meynell, A. C. B. Jayich, H. Park *et al.*, Signal amplification in a solid-state quantum sensor via asymmetric time-reversal of many-body dynamics, arXiv:2503.14598.

[28] L. Childress and R. Hanson, Diamond NV centers for quantum computing and quantum networks, MRS Bull. **38**, 134 (2013).

[29] Y. Cui, W.-H. Leong, G. Zhu, R.-B. Liu, and Q. Li, Nanodiamond-based spatial–temporal deformation sensing for cell mechanics, ACS Nano **19**, 13740 (2025).

[30] X. Feng, W.-H. Leong, K. Xia, C.-F. Liu, G.-Q. Liu, T. Rendler, J. Wrachtrup, R.-B. Liu, and Q. Li, Association of nanodiamond rotation dynamics with cell activities by translation-rotation tracking, Nano Lett. **21**, 3393 (2021).

[31] A. S. Barnard, Diamond standard in diagnostics: Nanodiamond biolabels make their mark, Analyst **134**, 1751 (2009).

[32] R. Schirhagl, K. Chang, M. Loretz, and C. L. Degen, Nitrogen-vacancy centers in diamond: Nanoscale sensors for physics and biology, Annu. Rev. Phys. Chem. **65**, 83 (2014).

[33] N. Aslam, H. Zhou, E. K. Urbach, M. J. Turner, R. L. Walsworth, M. D. Lukin, and H. Park, Quantum sensors for biomedical applications, Nat. Rev. Phys. **5**, 157 (2023).

[34] H. Yukawa, H. Kono, H. Ishiwata, R. Igarashi, Y. Takakusagi, S. Arai, Y. Hirano, T. Suhara, and Y. Baba, Quantum life science: Biological nano quantum sensors, quantum technology-based hyperpolarized MRI/NMR, quantum biology, and quantum biotechnology, Chem. Soc. Rev. **54**, 3293 (2025).

[35] K. Fang, V. M. Acosta, C. Santori, Z. Huang, K. M. Itoh, H. Watanabe, S. Shikata, and R. G. Beausoleil, High-sensitivity magnetometry based on quantum beats in diamond nitrogen-vacancy centers, Phys. Rev. Lett. **110**, 130802 (2013).

[36] A. Gruber, A. Dräbenstedt, C. Tietz, L. Fleury, J. Wrachtrup, and C. Borczyskowski, Scanning confocal optical microscopy and magnetic resonance on single defect centers, Science **276**, 2012 (1997).

[37] P. Kukura, H. Ewers, C. Müller, A. Renn, A. Helenius, and V. Sandoghdar, High-speed nanoscopic tracking of the position and orientation of a single virus, Nat. Methods **6**, 923 (2009).

[38] L. P. McGuinness, Y. Yan, A. Stacey, D. A. Simpson, L. T. Hall, D. Maclaurin, S. Prawer, P. Mulvaney, J. Wrachtrup, F. Caruso, R. E. Scholten, and L. C. L. Hollenberg, Quantum measurement and orientation tracking of fluorescent nanodiamonds inside living cells, Nat. Nanotechnol. **6**, 358 (2011).

[39] K. Shimabukuro, R. Yasuda, E. Muneyuki, K. Y. Hara, K. Kinosita Jr., and M. Yoshida, Catalysis and rotation of F_1 motor: Cleavage of ATP at the catalytic site occurs in 1 ms before 40° substep rotation, Proc. Natl. Acad. Sci. U. S. A. **100**, 14731 (2003).

[40] K. Fukushige, H. Kawaguchi, K. Shimazaki, T. Tashima, H. Takashima, and S. Takeuchi, Identification of the orientation of a single NV center in a nanodiamond using a three-dimensionally controlled magnetic field, Appl. Phys. Lett. **116**, 264002 (2020).

[41] R. Igarashi, T. Sugi, S. Sotoma, T. Genjo, Y. Kumiya, E. Walinda, H. Ueno, K. Ikeda, H. Sumiya, H. Tochio, Y. Yoshinari, Y. Harada, and M. Shirakawa, Tracking the 3D rotational dynamics in nanoscopic biological systems, J. Am. Chem. Soc. **142**, 7542 (2020). pMID: 32285668

[42] T. F. Segawa and R. Igarashi, Nanoscale quantum sensing with nitrogen-vacancy centers in nanodiamonds—a magnetic resonance perspective, Prog. Nucl. Magn. Reson. Spectrosc. **134–135**, 20 (2023).

[43] G. C. Papaefthymiou, The Mössbauer and magnetic properties of ferritin cores, Biochim. Biophys. Acta **1800**, 886 (2010). ferritin: Structures, Properties and Applications.

[44] S. M. Dubiel, B. Zablotna-Rypien, J. B. Mackey, and J. M. Williams, Magnetic properties of human liver and brain ferritin, Eur. Biophys. J. **28**, 263 (1999).

[45] See Supplemental Material at http://link.aps.org/supplemental/10.1103/zh44-55ms for sample preparation, reconstruction details, additional simulations, and cross-particle consistency checks, which includes Ref. [64].

[46] S. Felton, A. M. Edmonds, M. E. Newton, P. M. Martineau, D. Fisher, D. J. Twitchen, and J. M. Baker, Hyperfine interaction in the ground state of the negatively charged nitrogen vacancy center in diamond, Phys. Rev. B **79**, 075203 (2009).

[47] M. W. Doherty, N. B. Manson, P. Delaney, F. Jelezko, J. Wrachtrup, and L. C. Hollenberg, The nitrogen-vacancy colour centre in diamond, Phys. Rep. **528**, 1 (2013).

[48] The MathWorks, Inc., *Global Optimization Toolbox User's Guide: MultiStart* (MathWorks, Natick, MA, USA, 2025), accessed: July 2, 2025.

[49] A. Chulliat, W. Brown, M. Nair, N. Gómez Pérez, L.-Y. Young, C. Watson, N. Boneh, C. Beggan, B. Meyer, and M. Paniccia, The US/UK world magnetic model for 2025-2030: Technical report, Technical Report, National Centers for Environmental Information (NOAA) and British Geological Survey, 2025, geomagnetic field values at the measurement site are archived in the supplemental data (GitHub repository).

[50] G. Balasubramanian, P. Neumann, D. Twitchen, M. Markham, R. Kolesov, N. Mizuochi, J. Isoya, J. Achard, J. Beck, J. Tissler, V. Jacques, P. R. Hemmer, F. Jelezko, and J. Wrachtrup, Ultralong spin coherence time in isotopically engineered diamond, Nat. Mater. **8**, 383 (2009).

[51] A. Laraoui and C. A. Meriles, Approach to dark spin cooling in a diamond nanocrystal, ACS Nano **7**, 3403 (2013).

[52] H. S. Knowles, D. M. Kara, and M. Atatüre, Observing bulk diamond spin coherence in high-purity nanodiamonds, Nat. Mater. **13**, 21 (2014).

[53] K. Jensen, V. M. Acosta, A. Jarmola, and D. Budker, Light narrowing of magnetic resonances in ensembles of nitrogen-vacancy centers in diamond, Phys. Rev. B **87**, 014115 (2013).

[54] J.-P. Tetienne, T. Hingant, L. Rondin, A. Cavaillès, L. Mayer, G. Dantelle, T. Gacoin, J. Wrachtrup, J.-F. Roch, and V. Jacques, Spin relaxometry of single nitrogen-vacancy defects in diamond nanocrystals for magnetic noise sensing, Phys. Rev. B **87**, 235436 (2013).

[55] W. K. Lo, Y. Zhang, H. Y. Chow, J. Wu, M. Y. Leung, K. O. Ho, X. Du, Y. Chen, Y. Shen, D. Pan, and S. Yang, Enhancement of quantum coherence in solid-state qubits via interface engineering, Nat. Commun. **16**, 5984 (2025).

[56] J. M. Schloss, J. F. Barry, M. J. Turner, and R. L. Walsworth, Simultaneous broadband vector magnetometry using solid-state spins, Phys. Rev. Appl. **10**, 034044 (2018).

[57] F. Münzhuber, F. Bayer, V. Marković, J. Brehm, J. Kleinlein, L. W. Molenkamp, and T. Kiessling, Polarization-assisted vector magnetometry with no bias field using an ensemble of nitrogen-vacancy centers in diamond, Phys. Rev. Appl. **14**, 014055 (2020).

[58] P. Dubey, S. Kumar, C. Singh, J. Naliyapara, M. A. Poojar, K. B. Hari Krishnan, A. Poonia, and P. Peddibhotla, Magnetic field orientation dependence of continuous-wave optically detected magnetic resonance with nitrogen-vacancy ensembles, Appl. Magn. Reson. **57**, 6 (2026).

[59] K. Yamamoto, K. Ogawa, M. Tsukamoto, Y. Ashida, K. Sasaki, and K. Kobayashi, Nanodiamond quantum thermometry assisted with machine learning, Appl. Phys. Express **18**, 025001 (2025).

[60] A. Dréau, M. Lesik, L. Rondin, P. Spinicelli, O. Arcizet, J.-F. Roch, and V. Jacques, Avoiding power broadening in optically detected magnetic resonance of single NV defects for enhanced dc magnetic field sensitivity, Phys. Rev. B **84**, 195204 (2011).

[61] S. Kitazawa, Y. Matsuzaki, S. Saijo, K. Kakuyanagi, S. Saito, and J. Ishi-Hayase, Vector-magnetic-field sensing via multifrequency control of nitrogen-vacancy centers in diamond, Phys. Rev. A **96**, 042115 (2017).

[62] G. de Lange, Z. H. Wang, D. Ristè, V. V. Dobrovitski, and R. Hanson, Universal dynamical decoupling of a single solid-state spin from a spin bath, Science **330**, 60 (2010).

[63] S. Gider, D. D. Awschalom, T. Douglas, S. Mann, and M. Chaparala, Classical and quantum magnetic phenomena in natural and artificial ferritin proteins, Science **268**, 77 (1995).